Research Square

Preprints are preliminary reports that have not undergone peer review.
They should not be considered conclusive, used to inform clinical practice,
or referenced by the media as validated information.

Apollo active seismic experiments reveal 2D mechanical heterogeneity of the shallow lunar subsurface

Ginji Eshima
The University of Tokyo
Takeshi Tsuji
tsuji@sys.t.u-tokyo.ac.jp

The University of Tokyo

Article

Keywords:

Posted Date: November 3rd, 2026

DOI: https://doi.org/10.21203/rs.3.rs-11391753/v1

License: This work is licensed under a Creative Commons Attribution 4.0 International License.
Read Full License

Additional Declarations: No competing interests reported.

Abstract

The mechanical properties of the shallow lunar subsurface remain poorly constrained, despite their importance for understanding lunar evolution and for designing future surface infrastructure. Here, we reanalyze Apollo Active Seismic Experiment (ASE) data to image the shallow subsurface beneath the Apollo 16 landing site and compare it with Apollo 14. Because conventional surface-wave analysis is challenging for the Apollo ASE records owing to their limited signal-to-noise ratio and complex waveforms, we use a continuous-wavelet-transform multichannel surface-wave method (CWT-MASW) to robustly extract surface-wave dispersion and estimate two-dimensional S-wave velocity. The resulting model reveals pronounced lateral heterogeneity within the uppermost ~ 10 m. At a depth of 5 m, S-wave velocity varies from approximately 70 to 110 m/s over horizontal distances of only several tens of meters. This lateral variation is greater than the difference between the mean shallow structures at the Apollo 14 and Apollo 16 sites, demonstrating that substantial mechanical heterogeneity can occur even within a single landing area. Importantly, the tens-of-meters scale of the heterogeneity resolved here is comparable to the dimensions of individual future lunar infrastructure sites. These findings provide new constraints on the mechanical evolution of the lunar near surface and highlight the need for site-specific subsurface characterization in planning future lunar bases and associated infrastructure.

INTRODUCTION

The spatial heterogeneity of the mechanical properties of the uppermost formation (e.g. 0 ~ 10 m) of the Moon remains poorly constrained. The geological structure of this shallow subsurface has been shaped by billions of years of impact cratering, ejecta emplacement, fragmentation, and regolith gardening, and thus provides a window into the geological evolution of the lunar near surface (McKay et al., 1991;Speyerer et al., 2016) [1,2]. At the same time, the shallow subsurface is directly relevant to the next phase of lunar exploration, which is shifting from short-duration visits toward sustained human presence and, ultimately, the establishment of a Moon base (NASA, 2026) [3]. The Artemis program and related international efforts envision infrastructure such as habitats, landing pads, transportation systems, and facilities for in situ resource utilization. The design and stability of such infrastructure will depend critically on the geomechanical properties of the underlying regolith, including its stiffness, strength, density, and bearing capacity (Li et al., 2024)[4]. Some facilities, including astronomical observatories and resource-utilization systems, may also require precise ground leveling, making knowledge of subsurface mechanical properties important for site preparation and construction (Just et al., 2020)[5]. Regolith thickness, lateral continuity, and elastic properties may also influence access to subsurface resources, including water ice (Zhang et al., 2023) [6].

Active-source seismic exploration provides a direct means of characterizing the shallow subsurface, and surface-wave analysis is particularly valuable because S-wave velocity (V_s) from surface-wave analysis is closely related to shear rigidity and other mechanical properties (Socco et al., 2010; Park et al., 1999; Imazato et al., 2023) [7,8,9]. The Apollo missions provide the only active-source seismic measurements

acquired directly on the lunar surface. Active Seismic Experiments (ASEs) conducted during the Apollo 14, 16, and 17 missions yielded fundamental constraints on the shallow lunar subsurface (Kovach et al., 1971, 1972, 1976) [10,11,12]. Early analyses based primarily on seismic travel times established a basic stratigraphic framework in which a low-velocity regolith layer overlies mechanically more competent material (Watkins and Kovach, 1972; Kovach et al., 1972)[11, 13]. These studies, however, focused predominantly on P-wave velocities and generally represented the subsurface using one-dimensional, laterally homogeneous models. Recent tomographic analysis revealed 2D P-wave velocity structure at the Apollo landing sites (Villanova et al., 2025) [14], providing important constraints on lateral variations in shallow structure. However, the corresponding lateral variability in V_s, and thus in shear rigidity, remains unresolved. Consequently, despite the importance of shallow mechanical heterogeneity for both lunar science and future exploration, its lateral variability at scales of tens of meters remains poorly constrained.

Surface-wave dispersion provides a direct means of resolving the depth dependence of V_s in the shallow subsurface. In addition to constraining mechanical structure, V_s may provide information on subsurface volatiles: even a small amount of ice within lunar regolith can substantially increase V_s (Tsuji et al., 2023) [15]. Furthermore, combining P-wave velocity (V_p) and V_s can, in principle, provide additional constraints on elastic properties such as Poisson's ratio (Kunimasu et al., 2023) [16]. Previous studies have used Apollo seismic records to constrain lunar $V_s$structure. Larose et al. (2005) [17] and Tanimoto et al. (2008) [18] analyzed passive seismic records from Apollo 17, whereas Dal Moro (2015) [19] applied surface-wave analysis to data from the Apollo 14 and 16 sites. More recently, Imazato et al. (2023)[9] applied multichannel analysis of surface waves (MASW) to Apollo 14 active-source data and obtained a V_s profile that increases gradually from approximately 50 m/s near the surface to approximately 100 m/s at a depth of ~ 10 m. However, the limited source–receiver coverage allowed only a 1D representation of the shallow V_s structure, leaving its lateral variability unresolved.

The Apollo 16 ASE provides a unique opportunity to recover this missing spatial dimension. Unlike the Apollo 14 data available for surface-wave analysis, the Apollo 16 experiment includes numerous thumper shots distributed along a seismic profile. The resulting source–receiver combinations enable surface-wave dispersion to be evaluated at multiple positions along the profile and thereby allow the construction of a two-dimensional (2D) V_s model. This geometry provides a means to resolve not only the depth dependence of regolith properties but also lateral heterogeneity over scales of tens of meters —spatial scales relevant to local impact modification, regolith development, and future Moon-base site characterization.

A comparison between the Apollo 14 and Apollo 16 landing sites further provides a natural experiment for examining how contrasting lunar geological settings are expressed in shallow elastic structure. Apollo 14 landed on the Fra Mauro Formation, which is interpreted as ejecta associated with the formation of the Imbrium basin (Swann et al., 1977) [20]. Apollo 16, by contrast, explored the Descartes Highlands, an ancient highland terrain that has experienced prolonged impact modification and contains

abundant crater ejecta and regolith developed over billions of years (Apollo Field Geology Investigation Team, 1973; Hodges and Muehlberger, 1981; Stöffler et al. 1985) [21,22,23]. Resolving and comparing the shallow V_s structures at these two sites can therefore provide insight into how distinct geological histories influence the present-day mechanical properties of the lunar near surface.

Here, we reanalyzed the Apollo 16 ASE data using a surface-wave approach to construct 2D S-wave velocity model of the uppermost ~ 10 m of the lunar subsurface. Because conventional surface-wave analysis was difficult to apply to these noise-dominated data, we employed multichannel analysis of surface waves based on the continuous wavelet transform (CWT-MASW; Ikeda and Tsuji, 2019; Imazato et al., 2023) [9,24]. We further compared the resulting structure with that derived from the Apollo 14 ASE data. Our analysis reveals pronounced lateral variations in $V_s$at the Apollo 16 landing site, while the shallow velocity structures at Apollo 14 and Apollo 16 are broadly similar.

RESULTS

2D S-wave velocity structure at Apollo 16 site

The Apollo 16 Active Seismic Experiment (ASE) consisted of 19 thumper shots distributed along an approximately 90-m-long profile and three geophones located at 0, 45.7, and 91.4 m along the profile (Fig. 1a;Kovach et al., 1972) [11]. This geometry provides multiple source–receiver combinations that enable spatially distributed surface-wave analysis along the profile. Representative raw records show systematic variations in arrival time with source–receiver offset, although some short-offset records exhibit strong early-time amplitude saturation (Figs. 1b,1c).

The long-duration thumper source wavelet complicates direct surface-wave dispersion analysis of the original seismic records (Fig. 1). We therefore applied seismic interferometry (Wapenaar, 2004) [25] to retrieve approximate impulsive responses. Because some Apollo records exhibit amplitude saturation and variable amplitude fidelity, we used complex coherence rather than conventional cross-correlation, thereby emphasizing phase consistency while reducing sensitivity to amplitude variations and localized noise (Nakata et al., 2011) [26]. The resulting receiver gathers show coherent dispersive surface waves across a range of source–receiver offsets (Fig. 2).

For each receiver gather, surface-wave dispersion was analyzed using a moving window of six adjacent traces (Fig. 3). A dispersion curve was estimated for each window, which was then shifted along the shot sequence to obtain spatially distributed measurements along the seismic profile. Each dispersion curve was assigned to the center of the corresponding six-trace window. This procedure yielded 27 Rayleigh-wave phase-velocity dispersion curves across the Apollo 16 survey line. The wave packets analyzed in this study exhibit frequency-dependent dispersion, supporting their interpretation as surface waves. Each dispersion curve was independently inverted for a 1D V_s profile using a genetic algorithm (GA) (Tsuji et al., 2012) [27]. In the inversion, the theoretical Rayleigh-wave dispersion curves were calculated for candidate layered models and compared with the observed dispersion curves. Finally, 27

profiles were combined to construct the final 2D V_s model (Fig. 4a). Details of the GA inversion, model parameterization, and sensitivity analysis are provided in Materials and Methods.

To examine whether the apparent lateral velocity variations could result from Moon surface topography, furthermore, we additionally constructed an elevation-referenced representation of the 2D model. The individual 1D velocity profiles were positioned relative to surface elevations derived from the Lunar Reconnaissance Orbiter Camera (LROC) Narrow Angle Camera digital terrain model (NAC DTM2 m/post; Robinson et al., 2010; Henriksen et al., 2017) [28,29] (Fig. 4b). Elevation at geophone #3 (or Shot #1 in Fig. 1) was used as the reference level, and each 1D velocity profile was vertically positioned according to its local surface elevation. The observed heterogeneity therefore cannot be explained simply by topographic variations along the seismic profile.

The resulting 2D model reveals a shallow structure characterized by both a systematic increase in V_s with depth and pronounced lateral variability along the approximately 60 m long V_s profile (Fig. 4). Relatively low velocities (40-60m/s) can be observed near the surface across most of the profile, whereas V_s generally increases downward. This increase, however, is not spatially uniform. The velocity–depth gradients and absolute velocities vary among the inverted profiles, demonstrating that the shallow subsurface cannot be represented by a single laterally homogeneous velocity–depth function, such as terrestrial sedimentary formation. The lateral variability becomes particularly apparent at deeper than ~ 5 m. At depths of 5 m, V_s varies from approximately 70 to 110 m/s along the ~ 60-m survey line, corresponding to a lateral variation of approximately 40% over distances of only tens of meters. The resulting structure contains laterally alternating regions of relatively high and low V_s, rather than a simple set of continuous horizontal layers.

The depth range over which these features can be interpreted is constrained by Rayleigh-wave sensitivity to V_s (Fig. 5). Sensitivity is concentrated at shallow depths for higher frequencies and extends progressively deeper toward lower frequencies. For most selected profiles, the dispersion measurements provide useful constraints through several meters and, under favorable conditions, to 6–12 m or slightly deeper. Sensitivity decreases rapidly below this range. We therefore restrict interpretation of the velocity model to depth intervals supported by the sensitivity analysis and exclude poorly constrained regions.

Comparison of S-wave velocity structures at Apollo 14 and 16 sites

Apollo 14 ASE data were analyzed separately to obtain a 1D V_s profile for comparison with Apollo 16 (Fig. 6). Surface-wave dispersion was obtained from a multichannel gather following the approach of Imazato et al. (2023) [9] (red dashed line in Fig. 6), and the resulting dispersion curve was inverted using the same genetic-algorithm (GA) framework applied to the Apollo 16 data (red solid line in Fig. 6). The V_s profile obtained using the GA framework shows a similar overall trend to that of Imazato et al. (2023)

[9], although the estimated velocities are slightly higher, likely reflecting differences in the inversion setup, including the initial model and model parameterization (e.g., layer number).

Despite their different geological settings, Apollo 14 and Apollo 16 exhibit broadly similar V_s structures in the shallow subsurface. In particular, within the uppermost ~ 2 m, where the surface-wave data provide the strongest constraints, V_s is nearly identical at the two sites. The mean Apollo 16 profile shows slightly higher velocities than the Apollo 14 profile at greater depths, but this difference is small relative to the lateral variability observed along the Apollo 16 profile. Indeed, the lower-velocity portions of the Apollo 16 profile exhibit V_s values comparable to, or locally lower than, the Apollo 14 profile. Thus, the range of V_s observed laterally within Apollo 16 survey line exceeds the difference between the Apollo 14 profile and the mean Apollo 16 profile. However, this comparison should be interpreted with caution because the Apollo 14 result is based on a single 1D V_s profile and does not resolve lateral variability.

DISCUSSION

Spatial heterogeneity of the lunar near-surface structure

The pronounced lateral variations in V_s at Apollo 16 site indicate that the shallow lunar subsurface is mechanically heterogeneous over horizontal distances of only tens of meters. Such heterogeneity could be explained by the long history of impact modification of the Descartes Highlands. Impact cratering, excavation, ejecta emplacement, fragmentation, and regolith gardening can generate spatial variations in regolith thickness, porosity, compaction, particle contacts, and the abundance and distribution of buried rock fragments (Apollo Field Geology Investigation Team, 1973; Hodges and Muehlberger, 1981; Spudis, 1984) [21,22,30]. Impacts producing craters tens to hundreds of meters in diameter can further excavate and redistribute near-surface materials over comparable spatial scales (Mahanti et al., 2018) [31]. Although the resolution of our surface-wave analysis is insufficient to associate individual velocity anomalies with specific craters or ejecta deposits, the observed heterogeneity is consistent with the cumulative effects of these impact-driven processes. A single 1D velocity profile may therefore not adequately represent the shallow mechanical structure even within an individual lunar landing site.

The similarity of the shallow V_s structures at Apollo 14 and Apollo 16 is notable given their distinct geological settings. Apollo 14 landed on the Fra Mauro Formation, dominated by material associated with the Imbrium basin ejecta (Swann, 1977) [20], whereas Apollo 16 explored the ancient Descartes Highlands, which experienced a different history of impact modification (Apollo Field Geology Investigation Team, 1973; Hodges and Muehlberger, 1981) [21,22]. The nearly constant, low V_s (~ 50m/s) within the uppermost ~ 2 m at both sites may represent a mechanically weak and relatively homogeneous surficial regolith layer. Previous Apollo seismic studies similarly inferred very low shear-wave velocities near the lunar surface, followed by a gradual or stepwise increase with depth (Mark and Sutton, 1975; Horvath et al., 1980; Larose et al., 2005) [17,32,33]. Such a structure is broadly consistent with

granular-layer models in which weak particle contacts and high porosity produce low seismic velocities near the surface, whereas increasing overburden pressure and compaction progressively stiffen the regolith at greater depth (Cooper et al., 1974) [34]. The similarity between the two sites may further suggest that repeated impact gardening produces broadly similar mechanical conditions in the uppermost regolith despite differences in regional geological setting.

The increasing V_s below ~ 2 m depth may reflect a gradual transition from highly disturbed surficial regolith to progressively more compacted or mechanically interconnected material. At greater depths, local variations in porosity, compaction, particle contacts, buried rock fragments, brecciation, and impact history may become increasingly important. Returned samples and in situ measurements show broad and overlapping grain-size distributions at the Apollo 14 and Apollo 16 sites (Graf, 1993) [35], substantial sample-to-sample variability (Heiken et al., 1973) [36], and vertical and lateral variations in bulk density and other soil properties (Mitchell et al., 1972a, 1972b) [37,38]. The seismic results therefore suggest a depth-dependent structure in which the uppermost regolith has broadly similar mechanical properties across the two landing sites, whereas greater spatial variability develops at depth as local geological and impact processes become more influential.

Previous analyses of the Apollo active-source data have also estimated shallow P-wave velocity structures, potentially providing complementary constraints on the elastic properties of the lunar near surface (Martella et al., 2022; Villanova et al., 2025) [14,39]. Direct comparison with V_s structure obtained in this study, however, requires caution because the P- and S-wave models were derived independently using different analysis methods and have different spatial sensitivities and resolutions. In particular, the P-wave structure at the landing site was constrained mainly from refracted arrivals, and the shallowest reported P-wave velocity along the sampled refracted-wave paths is 104 m/s (Kovach et al., 1972) [11]. Therefore, because the P- and S-wave velocity models sample different parts of the shallow subsurface and have different effective resolutions, they cannot be straightforwardly combined to derive reliable elastic parameters. Although the V_s estimated in this study are locally comparable in magnitude to previously reported shallow P-wave velocities, the wavefield analyzed in this study exhibits clear frequency-dependent dispersion, supporting its interpretation as surface waves rather than direct or refracted P waves.

Implications for lunar exploration and infrastructure

The shallow subsurface will play a critical role in sustained lunar exploration and future infrastructure development. Habitats, landing pads, roads, astronomical observatories, excavation systems, and facilities for in situ resource utilization will interact directly with the uppermost several to tens of meters of the lunar subsurface. Their construction, operation, and long-term stability will therefore depend on local geotechnical conditions, including regolith thickness, stiffness, compaction, and the presence of mechanically heterogeneous layers or buried blocks. Our Apollo 16 results show that shallow V_s structure can vary substantially over horizontal distances of only tens of meters (Fig. 4), a spatial scale

comparable to that of individual infrastructure sites. Geological or geotechnical properties inferred at one location may therefore not be representative of even a nearby site. This finding highlights the importance of site-specific characterization rather than relying solely on regional geological information when evaluating future lunar infrastructure sites.

The active-source surface-wave approach demonstrated here is well suited to characterizing heterogeneity at these spatial scales under the limited source–receiver configurations expected in lunar exploration (Nunn et al., 2020; Imazato et al., 2023; Tsuji et al., 2023, 2026) [9,15,40,41]. Surface waves provide direct constraints on shallow V_s and can be generated and recorded using relatively compact sources and sparse receiver deployments. Higher-frequency body-wave observations could complement these measurements by providing constraints on P-wave velocity, sharper layer boundaries, and smaller-scale heterogeneity. Combining surface- and body-wave observations could therefore provide complementary constraints on the mechanical structure of potential lunar infrastructure sites.

Future lunar active-seismic exploration will require compact, repeatable sources and lightweight receivers that can operate under severe mass, power, and deployment constraints (Nunn et al., 2020) [40]. Broadband and reproducible source signals would enable complementary surface-wave, refraction, reflection, and potentially waveform-based analyses. Recent developments in compact active sources, including the Portable Active Seismic Source (PASS), demonstrate the feasibility of generating repeatable seismic signals with instruments suitable for astronaut- or rover-based deployment (Tsuji et al., 2026) [41]. In parallel, distributed acoustic sensing has been proposed as a promising means of providing dense seismic sampling on the Moon, although deployment and coupling remain important technical challenges (Zhai et al., 2024) [42]. Combining such emerging source and receiver technologies could enable flexible active-seismic surveys for site-specific characterization of the lunar near surface. The Apollo results analyzed here therefore provide not only constraints on lunar shallow structure, but also a valuable reference for designing the source characteristics, receiver geometry, and analysis strategies required for future lunar seismic exploration.

MATERIALS and METHODS

Active seismic experiment (ASE) data

We analyzed active-source seismic data acquired during the Apollo 16 and Apollo 14 missions. The Apollo 16 dataset was used to resolve the 2D V_s structure, whereas the Apollo 14 dataset was analyzed separately to obtain a 1D V_s profile for comparison.

The Apollo 16 ASE was conducted on 21 April 1972 (NASA, 1972; Brzostowski and Brzostowski, 2009) [43,44] and consisted of 19 thumper shots and three geophones distributed along an approximately 90 m-long profile. G3, G2, and G1 were located at 0, 45.7, and 91.4 m along the profile, respectively (Fig. 1a). The dataset therefore contains multiple source–receiver combinations spanning the profile. Several

short-offset records exhibit strong amplitude saturation, particularly the G3 record from shot 1 and the G1 record from shot 19 (Fig. 1c).

For Apollo 14, we used the same active-source seismic dataset analyzed by Imazato et al. (2023). The ASE data were acquired on 6 February 1971 using a thumper source and three geophones (Kovach et al., 1971) [10]. Following Imazato et al. (2023), we used the virtual multichannel gather constructed from eight thumper shots recorded by geophones G1 and G2.

Construction of receiver gathers

Conventional multichannel surface-wave surveys typically use multiple receivers to sample wave propagation along a profile (i.e., shot gather). The Apollo 16 ASE, however, included only three geophones but 19 thumper shot locations. We therefore analyzed the data as receiver gathers, using the multiple shot locations to provide spatial sampling along the profile. For each gather, records from multiple thumper shots were assembled for a fixed geophone. Owing to source–receiver reciprocity, the resulting receiver gathers can be analyzed in the same manner as conventional shot gathers for surface-wave dispersion analysis. Receiver gathers were constructed for each of the three geophones (G1, G2, and G3; Fig. 2). For G1 and G3, located near opposite ends of the profile, each gather contained up to 19 traces. Because G2 is located near the center of the profile, its records were separated by propagation direction into west-northwest (WNW; toward G3) and east-southeast (ESE; toward G1) gathers, containing up to 11 and 9 traces, respectively.

Because the long-duration source wavelet complicates direct surface-wave dispersion analysis, we used seismic interferometry to retrieve an approximate impulsive response for each receiver gather. For each geophone, a nearby shot with a clear signal and minimal amplitude saturation was selected as the reference. Some Apollo 16 records, particularly those acquired at very short source–receiver offsets, exhibit amplitude saturation (Fig. 1c; Villanova et al., 2025) [14]. At G3, shot 2 was selected as the reference instead of the colocated shot 1, which exhibits strong saturation (Fig. S1). Similarly, shot 18 was selected for G1 instead of the colocated shot 19. At G2, saturation of the colocated shot 11 was less severe, allowing shots 10, 11, and 12 to be evaluated as reference sources. We therefore constructed interferometric receiver gathers using shot 2 as the reference source for G3, shots 10, 11, and 12 for G2, and shot 18 for G1 (fig. S1).

Cross coherence was used for the interferometric processing to reduce sensitivity to variations in absolute amplitude and localized amplitude distortion, which is particularly advantageous for the ASE data because some records exhibit amplitude saturation near the shot locations (Nakata et al., 2011) [26]. The complex-coherence functions were transformed into the time domain over a frequency range of 5–22 Hz. The resulting gathers (Fig. 2) show relatively impulsive, coherent arrivals with systematic moveout as a function of offset, consistent with surface-wave propagation.

Calculation of surface wave dispersion

To obtain spatially localized estimates of Rayleigh-wave dispersion along the Apollo 16 profile, each receiver gather was divided into moving windows consisting of six adjacent traces. A dispersion curve was estimated from each six-trace window, after which the window was shifted along the shot sequence to obtain measurements at multiple positions. The representative horizontal position of each dispersion curve was defined as the center of the corresponding six-shot window. The six-trace window was selected as a compromise between depth sensitivity and lateral resolution. Resolving the velocity structure to depths of approximately 10 m requires a sufficiently long source–receiver aperture to constrain the lower-frequency components of the dispersion curve, whereas using a larger number of traces would broaden the spatial averaging and reduce lateral resolution. We also tested different window sizes and found that six traces provided relatively stable and continuous dispersion estimates while retaining sufficient spatial localization.

Because the relatively high noise level of the Apollo data makes conventional multichannel analysis of surface waves (MASW; Park et al., 1999) [8] challenging, we applied MASW based on the continuous wavelet transform (CWT-MASW; Ikeda and Tsuji, 2018, 2019; Imazato et al., 2023) [9,45]. CWT-MASW exploits the localization of dispersive wave packets in the time–frequency domain and estimates phase velocity using phase information around the group arrival (Imazato et al., 2023) [9]. This approach reduces the influence of noise outside the dominant surface-wave packet. A continuous dispersion trend interpreted as the fundamental Rayleigh-wave mode was manually picked from each spectrum (Fig. 3). In the G1 and G3 receiver gather, large source-receiver offsets resulted in poorly resolved dispersion trends, and these large-offset windows were excluded. This procedure yielded 27 Rayleigh-wave phase-velocity dispersion curves distributed along the Apollo 16 profile.

Inversion for 1D S-wave velocity profiles

Each phase-velocity dispersion curve was independently inverted to obtain a 1D V_s profile using a genetic algorithm (GA), following the general inversion framework of Tsuji et al. (2012) [27]. The subsurface was parameterized as a seven-layer model, with both V_s and layer thickness treated as unknown parameters. The seven layers initially spanned depths of 0–1, 1–2, 2–4, 4–6, 6–8, 8–10, and 10–12 m. The V_s values and layer thicknesses were allowed to vary within $\pm 30\%$ of their initial values. The total thickness of the seven-layer model was constrained to 12 m. The initial velocity model was constructed from the observed dispersion curve using the empirical one-third-wavelength approximation (Hayashi, 2008) [46], in which V_s is estimated as 1.1 times the observed Rayleigh-wave phase velocity and assigned to a depth equal to one-third of the corresponding wavelength. The resulting depth– V_s relation was sampled at the midpoints of each initial layer. At depths beyond those sampled by the observed dispersion curve, the initial $V_s$model was extrapolated using a linear velocity gradient.

For each candidate model generated by the GA, the theoretical fundamental-mode Rayleigh-wave dispersion curve was calculated using Computer Programs in Seismology (CPS; Herrmann, 2013) [47] and

compared with the observed phase velocities. For the forward calculation, $V_p$was determined from V_s assuming a constant V_p/V_s ratio of 1.71. This ratio was derived from a V_p of 94.0 m/s at 1.5-m depth in the Apollo 16 P-wave model of Villanova et al. (2025) [14] and the corresponding initial V_s of 54.90 m/s, and corresponds to a Poisson's ratio of approximately 0.24. Density was calculated from $V_p$using the Nafe–Drake velocity–density relationship (Ludwig et al., 1970) [48]. Sensitivity tests using alternative V_p/V_sratios and density values produced essentially the same $V_s$structure, indicating that the inversion results are insensitive to these assumptions within the tested ranges.

The misfit between the observed and predicted phase velocities was quantified using the root-mean-square error (RMSE), which served as the objective function for the GA optimization. The GA used a population of 20 candidate models evolved over 20 generations. Tournament selection was used to select models for reproduction, and mutation was implemented by adding small random perturbations drawn from a normal distribution to the model parameters. For each observed dispersion curve, the GA inversion was repeated 20 times using different random seeds, and the resulting 20 V_s models were averaged to obtain the final 1D V_s profile. Applying this procedure independently to the 27 dispersion curves yielded 27 1D V_s profiles distributed along the Apollo 16 seismic survey line.

Depth sensitivity and 2D model construction

We evaluated the depth sensitivity of each inverted 1D model using finite-difference sensitivity kernels for Rayleigh-wave phase velocity with respect to V_s. For each layer, V_s was perturbed by a small amount while all other model parameters were held fixed, and the resulting change in theoretical phase velocity was used to estimate the sensitivity to V_s. Because the objective was to determine the depth interval over which the model was constrained rather than the sign of the velocity response, we used the absolute value of the sensitivity kernels.

The reliable depth range for each 1D profile was determined from the depth interval over which the observed Rayleigh-wave phase velocities retained appreciable sensitivity to V_s over multiple frequencies (Fig. 5). Higher frequencies predominantly constrain the shallow subsurface, whereas progressively lower frequencies provide sensitivity at greater depths. Sensitivity generally decreases rapidly below approximately 6–12 m (Fig. 5), although the reliable depth range varies among profiles depending on the frequency range of the observed dispersion curves. Only V_s estimates within these profile-specific reliable depth ranges were retained for construction of the final 2D model (Fig. 4).

The retained $V_s$estimates were interpolated along the seismic profile using modified Akima piecewise cubic Hermite interpolation (Akima, 1970) [49] to construct the 2D $V_s$model (Fig. 4). Interpolation was restricted to the reliable depth range determined for each 1D profile from the sensitivity analysis described above. The interpolated model was subsequently smoothed in the horizontal and vertical directions to suppress interpolation-induced discontinuities.

Declarations

Competing interests:

The authors declare they have no competing interests.

Data, code, and materials availability:

The Apollo 14 and Apollo 16 Active Seismic Experiment (ASE) data analyzed in this study are publicly available through the Data Archives and Transmission System (DARTS) of the Institute of Space and Astronautical Science, Japan Aerospace Exploration Agency (ISAS/JAXA), under the dataset “Apollo Active Seismic Experiment Data” (https://darts.isas.jaxa.jp/datasets/apollo-ase-data). The data are available at the DARTS Apollo ASE data repository. The theoretical Rayleigh-wave dispersion curves used in the inversion were calculated using the publicly available Computer Programs in Seismology (CPS). This study did not generate any new materials.

Funding:

Japan Society for the Promotion of Science (JSPS) KAKENHI grant JP20H01997 (T.T.).

Author Contribution

Conceptualization of this study was carried out by T.T., while the methodology was developed by G.E. and T.T. The investigation was conducted by G.E. and T.T., and data analysis and visualization were performed by G.E. The study was supervised by T.T. The original draft was written by G.E., with review and editing performed by T.T. All authors have read and approved the final version of the manuscript.

Acknowledgments

We thank NASA for making the Apollo Active Seismic Experiment data publicly available. We also thank Matthew Brzostowski, Adam Brzostowski, and Yosio Nakamura for providing the Apollo active seismic observation data through the Data Archives and Transmission System (DARTS) of the Institute of Space and Astronautical Science, Japan Aerospace Exploration Agency (ISAS/JAXA).

References

1. D. S. McKay, G. Heiken, A. Basu, G. Blanford, S. Simon, R. Reedy, B. M. French, J. J. Papike, The lunar regolith, in *Lunar Sourcebook: A User’s Guide to the Moon*, G. H. Heiken, D. T. Vaniman, B. M. French, Eds. (Cambridge Univ. Press, 1991), pp. 285–356.
2. E. J. Speyerer, R. Z. Povilaitis, M. S. Robinson, P. C. Thomas, R. V. Wagner, Quantifying crater production and regolith overturn on the Moon with temporal imaging. *Nature* 538, 215–218 (2016).

doi:10.1038/nature19829.

3. National Aeronautics and Space Administration (NASA), Moon to Mars Architecture—Strategy and Objectives. https://www.nasa.gov/moontomarsarchitecture-strategyandobjectives/ (accessed 3 September 2026).
4. X. Li, Y. Gao, Y. Zhou, W. Han, C. Zhou, A review on design and construction of the lunar launch/landing infrastructure. *Adv. Space Res.* 74, 4030–4049 (2024). doi:10.1016/j.asr.2024.07.006.
5. G. H. Just, K. H. Smith, K. J. Joy, M. Roy, Parametric review of existing regolith excavation techniques for lunar In Situ Resource Utilisation (ISRU) and recommendations for future excavation experiments. *Planet. Space Sci.* 180, 104746 (2020).
6. P. Zhang, W. Dai, R. Niu, G. Zhang, G. Liu, X. Liu, Z. Bo, Z. Wang, H. Zheng, et al., Overview of the lunar in situ resource utilization techniques for future lunar missions. *Space Sci. Technol.* 3, 0037 (2023). doi:10.34133/space.0037.
7. L. V. Socco, S. Foti, D. Boiero, Surface-wave analysis for building near-surface velocity models—Established approaches and new perspectives. *Geophysics* 75, 75A83–75A102 (2010). doi:10.1190/1.3479491.
8. C. B. Park, R. D. Miller, J. Xia, Multichannel analysis of surface waves. *Geophysics* 64, 800–808 (1999). doi:10.1190/1.1444590.
9. H. Imazato, T. Ikeda, T. Tsuji, Shallow S wave velocity profile from active source seismic data at the Apollo 14 landing site based on virtual multichannel analysis of surface waves. *Icarus* 406, 115724 (2023). doi:10.1016/j.icarus.2023.115724.
10. R. L. Kovach, J. S. Watkins, T. Landers, Active seismic experiment, in *Apollo 14 Preliminary Science Report*, NASA SP-272 (National Aeronautics and Space Administration, 1971), Chap. 7, pp. 163–174.
11. R. L. Kovach, J. S. Watkins, P. Talwani, Active seismic experiment, in *Apollo 16 Preliminary Science Report*, NASA SP-315 (National Aeronautics and Space Administration, 1972), sect. 10, pp. 10-1-10–14.
12. R. L. Kovach, J. S. Watkins, P. Talwani, *Apollo 14 and 16 Active Seismic Experiments, and Apollo 17 Lunar Seismic Profiling*, NASA Contractor Report NASA-CR-147760 (National Aeronautics and Space Administration, 1976).
13. J. S. Watkins, R. L. Kovach, Apollo 14 active seismic experiment. *Science* 175, 1244–1245 (1972). doi:10.1126/science.175.4027.1244.
14. L. S. Villanova, E. Yokoyama, S. T. R. Maciel, Investigation into the lunar regolith layer using Apollo mission active seismic data. *Earth Planets Space* 77, 190 (2025). doi:10.1186/s40623-025-02244-3.
15. T. Tsuji, T. Kobayashi, J. Kinoshita, T. Ikeda, T. Uchigaki, Y. Nagata, T. Kawamura, K. Ogawa, S. Tanaka, A. Araya, Lunar active seismic profiler for investigating shallow substrates of the Moon and other extraterrestrial environments. *Icarus* 404, 115666 (2023). doi:10.1016/j.icarus.2023.115666.
16. T. Kunimasu, K. Sawayama, T. Tsuji, Estimation of the mass fraction and distribution of ice in a lunar regolith simulant from seismic velocity. *Icarus* 406, 115725 (2023).

doi:10.1016/j.icarus.2023.115725.

17. E. Larose, A. Khan, Y. Nakamura, M. Campillo, Lunar subsurface investigated from correlation of seismic noise. *Geophys. Res. Lett.* 32, L16201 (2005). doi:10.1029/2005GL023518.
18. T. Tanimoto, M. Eitzel, T. Yano, The noise cross-correlation approach for Apollo 17 LSPE data: Diurnal change in seismic parameters in shallow lunar crust. *J. Geophys. Res. Planets* 113, E08011 (2008). doi:10.1029/2007JE003016.
19. G. Dal Moro, Joint analysis of Rayleigh-wave dispersion and HVSR of lunar seismic data from the Apollo 14 and 16 sites. *Icarus* 254, 338–349 (2015). doi:10.1016/j.icarus.2015.03.017.
20. G. A. Swann, et al., *Geology of the Apollo 14 Landing Site in the Fra Mauro Highlands*, U.S. Geological Survey Professional Paper 880 (U.S. Government Printing Office, Washington, DC, 1977), 103 pp. doi:10.3133/pp880.
21. Apollo Field Geology Investigation Team, Apollo 16 exploration of Descartes: A geologic summary. *Science* 179, 62–69 (1973). doi:10.1126/science.179.4068.62.
22. C. A. Hodges, W. R. Muehlberger, *Geology of the Apollo 16 Area, Central Lunar Highlands*, U.S. Geological Survey Professional Paper 1048 (U.S. Government Printing Office, Washington, DC, 1981). doi:10.3133/pp1048.
23. D. Stöffler et al., Composition and evolution of the lunar crust in the Descartes Highlands, Apollo 16. *J. Geophys. Res.* 90, C449–C506 (1985). doi:10.1029/JB090iS02p0C449.
24. T. Ikeda, T. Tsuji, Multichannel analysis of surface waves with continuous wavelet transform for near surface applications, in *Fifth International Conference on Engineering Geophysics (ICEG), Al Ain, UAE, 21–24 October 2019* (Society of Exploration Geophysicists, 2019). doi:10.1190/iceg2019-012.1.
25. K. Wapenaar, Retrieving the elastodynamic Green's function of an arbitrary inhomogeneous medium by cross correlation. *Phys. Rev. Lett.* 93, 254301 (2004). doi:10.1103/PhysRevLett.93.254301.
26. N. Nakata, R. Snieder, T. Tsuji, K. Larner, T. Matsuoka, Shear wave imaging from traffic noise using seismic interferometry by cross-coherence. *Geophysics* 76, SA97–SA106 (2011). doi:10.1190/geo2010-0188.1.
27. T. Tsuji, T. A. Johansen, B. O. Ruud, T. Ikeda, T. Matsuoka, Surface-wave analysis for identifying unfrozen zones in subglacial sediments. *Geophysics* 77, EN17–EN27 (2012). doi:10.1190/GEO2011-0222.1.
28. M. S. Robinson, S. M. Brylow, M. Tschimmel, D. Humm, S. J. Lawrence, P. C. Thomas, B. W. Denevi, E. Bowman-Cisneros, J. Zerr, M. A. Ravine, M. A. Caplinger, F. T. Ghaemi, J. A. Schaffner, M. C. Malin, P. Mahanti, A. Bartels, J. Anderson, T. N. Tran, E. M. Eliason, A. S. McEwen, E. Turtle, B. L. Jolliff, H. Hiesinger, Lunar Reconnaissance Orbiter Camera (LROC) instrument overview. *Space Sci. Rev.* 150, 81–124 (2010). doi:10.1007/s11214-010-9634-2.
29. M. R. Henriksen, M. R. Manheim, K. N. Burns, P. Seymour, E. J. Speyerer, A. Deran, A. K. Boyd, E. Howington-Kraus, M. R. Rosiek, B. A. Archinal, M. S. Robinson, Extracting accurate and precise topography from LROC Narrow Angle Camera stereo observations. *Icarus* 283, 122–137 (2017). doi:10.1016/j.icarus.2016.05.012.

30. P. D. Spudis, Apollo 16 site geology and impact melts: Implications for the geologic history of the lunar highlands. *J. Geophys. Res.* 89, C95–C107 (1984). doi:10.1029/JB089iS01p00C95.
31. P. Mahanti, M. S. Robinson, T. J. Thompson, M. R. Henriksen, Small lunar craters at the Apollo 16 and 17 landing sites—Morphology and degradation. *Icarus* 299, 475–501 (2018). doi:10.1016/j.icarus.2017.08.018.
32. N. Mark, G. H. Sutton, Lunar shear velocity structure at Apollo sites 12, 14, and 15. *J. Geophys. Res.* 80, 4932–4938 (1975). doi:10.1029/JB080i035p04932.
33. P. Horvath, G. V. Latham, Y. Nakamura, H. J. Dorman, Lunar near-surface shear wave velocities at the Apollo landing sites as inferred from spectral amplitude ratios. *J. Geophys. Res.* 85, 6572–6578 (1980). doi:10.1029/JB085iB11p06572.
34. M. R. Cooper, R. L. Kovach, J. S. Watkins, Lunar near-surface structure. *Rev. Geophys.* 12(3), 291–308 (1974).
35. J. C. Graf, *Lunar Soils Grain Size Catalog*, NASA Reference Publication 1265 (National Aeronautics and Space Administration, 1993).
36. G. H. Heiken, D. S. McKay, R. M. Fruland, Apollo 16 soils: Grain size analyses and petrography, in *Proceedings of the Fourth Lunar Science Conference* 1, 251–265 (1973).
37. J. K. Mitchell, L. G. Bromwell, W. D. Carrier III, N. C. Costes, R. F. Scott, Soil mechanical properties at the Apollo 14 site. *J. Geophys. Res.* 77, 5641–5664 (1972a). doi:10.1029/JB077i029p05641.
38. J. K. Mitchell, W. D. Carrier III, W. N. Houston, R. F. Scott, L. G. Bromwell, H. T. Durgunoglu, H. J. Hovland, D. D. Treadwell, N. C. Costes, Soil mechanics, in *Apollo 16 Preliminary Science Report*, NASA SP-315 (National Aeronautics and Space Administration, 1972b), Chap. 8, pp. 8-1-8–29.
39. C. H. Martella, E. Mattei, S. E. Lauro, B. Cosciotti, E. Pettinelli, Combining active seismic data from Apollo 14 and 16 with ground penetrating radar results to examine the shallow lunar subsurface. *Planet. Space Sci.* 214, 105460 (2022). doi:10.1016/j.pss.2022.105460.
40. C. Nunn, R. F. Garcia, Y. Nakamura, A. G. Marusiak, T. Kawamura, D. Sun, L. Margerin, R. Weber, M. Drilleau, M. A. Wieczorek, A. Khan, A. Rivoldini, P. Lognonné, P. Zhu, Lunar seismology: A data and instrumentation review. *Space Sci. Rev.* 216, 89 (2020). doi:10.1007/s11214-020-00709-3.
41. T. Tsuji, K. Sakamoto, T. S. Imam, A. Kioka, Y. Takenaka, F. Murakami, H. Tsukahara, K. Ochi, S. Abe, S. Tanaka, T. Kawamura, Subsurface imaging with a voice-coil portable active seismic source and a single geophone: From field validation to lunar application. *Adv. Space Res.* 77, 8252–8266 (2026). doi:10.1016/j.asr.2026.02.037.
42. Q. Zhai, A. Husker, Z. Zhan, E. Biondi, J. Yin, F. Civilini, L. Costa, Assessing the feasibility of distributed acoustic sensing (DAS) for moonquake detection. *Earth Planet. Sci. Lett.* 631, 118606 (2024). doi:10.1016/j.epsl.2024.118606.
43. National Aeronautics and Space Administration, *Apollo 16 Mission Report*, MSC-07230 (Manned Spacecraft Center, Houston, TX, 1972).
44. M. Brzostowski, A. Brzostowski, Archiving the Apollo active seismic data. *Lead. Edge* 28, 414–416 (2009). doi:10.1190/1.3112756.

45. T. Ikeda, T. Tsuji, Surface-wave tomography for near-surface characterization with continuous wavelet transform for two-station cross-correlation, in *SEG Technical Program Expanded Abstracts 2018* (Society of Exploration Geophysicists, 2018), pp. 2531–2535. doi:10.1190/segam2018-2996939.1.
46. K. Hayashi, *Development of Surface-Wave Methods and Its Application to Site Investigations*, Ph.D. dissertation, Kyoto University (2008). doi:10.14989/doctor.k13774.
47. R. B. Herrmann, Computer programs in seismology: An evolving tool for instruction and research. *Seismol. Res. Lett.* 84, 1081–1088 (2013). doi:10.1785/0220110096.
48. W. J. Ludwig, J. E. Nafe, C. L. Drake, Seismic refraction, in *The Sea*, vol. 4, A. E. Maxwell, Ed. (Wiley-Interscience, 1970), pp. 53–84.
49. H. Akima, A new method of interpolation and smooth curve fitting based on local procedures. *J. ACM* 17, 589–602 (1970). doi:10.1145/321607.321609.

Figures

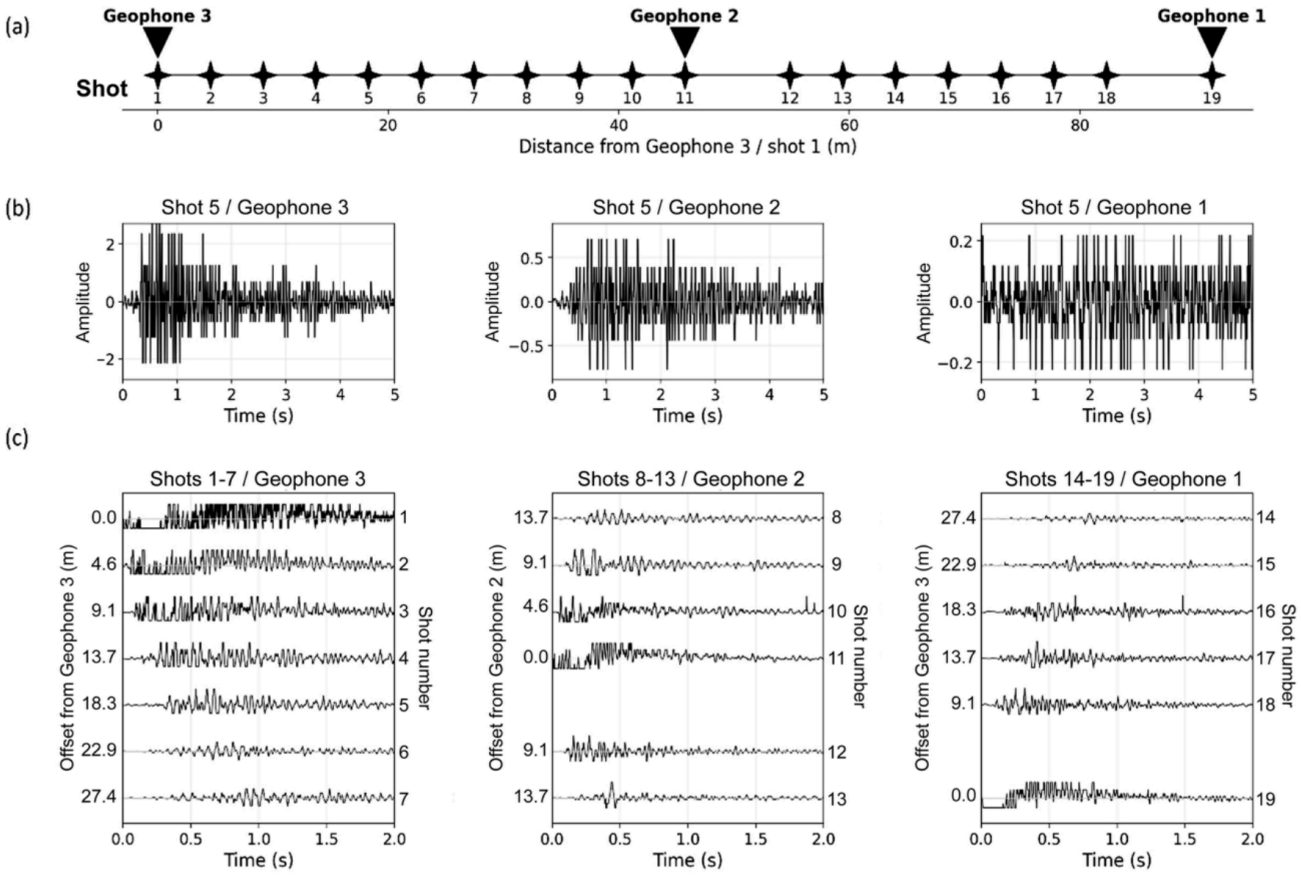


Figure 1

Apollo 16 ASE geometry and representative seismic records.

(A) Locations of the active-source shots and geophones used in the Apollo 16 ASE. Stars indicate shot locations, and triangles indicate geophone locations. Geophone 3 (G3), Geophone 2 (G2), and Geophone 1 (G1) are located at 0.0, 45.7, and 91.4 m along the profile, respectively. (B) Raw seismic records at G3, G2, and G1, generated by shot 5. Traces are shown at their recorded amplitudes without normalization. (C) Representative receiver gathers acquired at G3, G2, and G1. Strong early-time amplitude saturation is observed in some short-offset records, particularly the G3 record from shot 1 and the G1 record from shot 19.

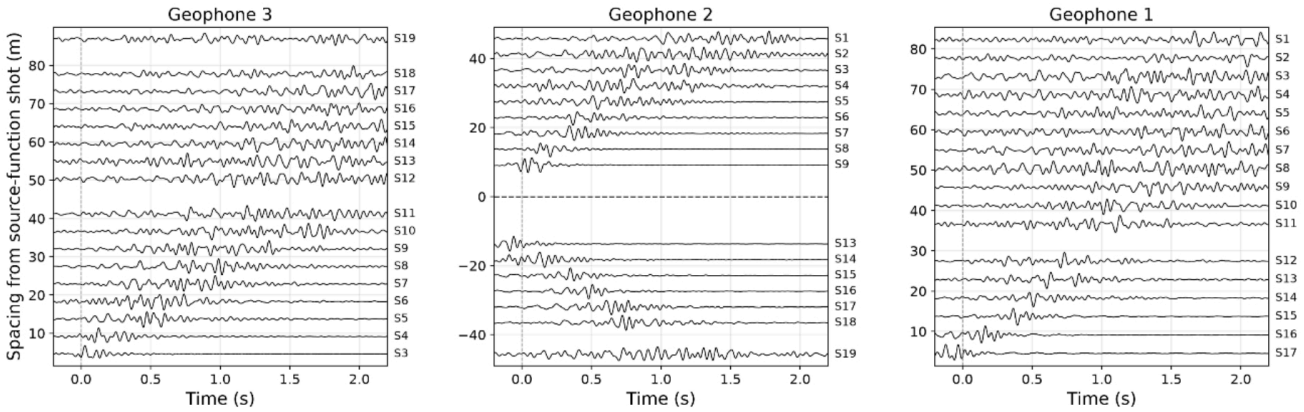


Figure 2

Representative receiver gathers constructed using cross coherence.
Each trace is normalized for display. Coherent wave packets show systematic moveout with increasing offset, consistent with dispersive surface-wave propagation.

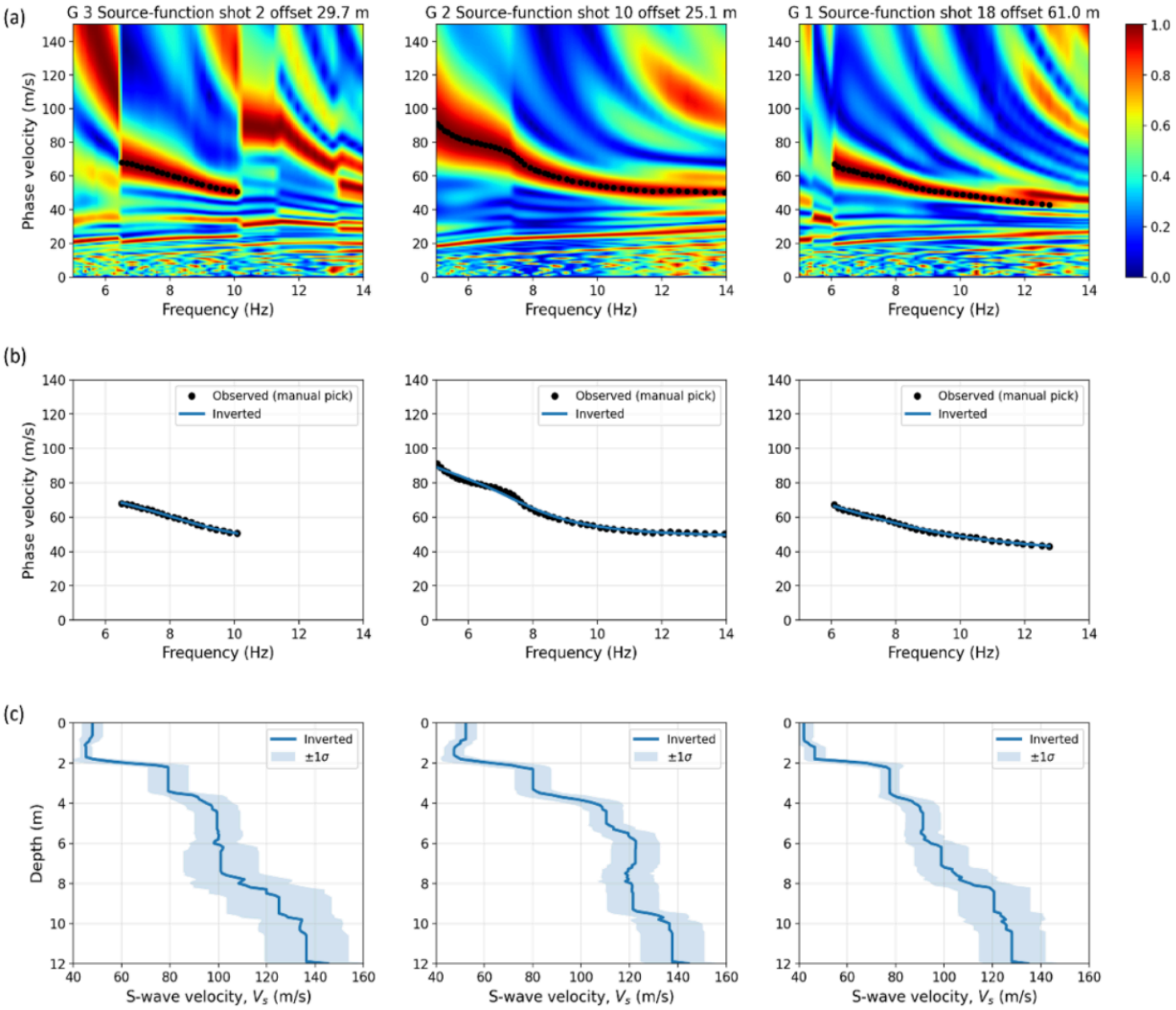


Figure 3

Rayleigh-wave dispersion measurements and inversion results.
(a) Representative dispersion curves obtained using CWT-MASW. Black dots indicate manually picked fundamental-mode Rayleigh-wave phase velocities. (b) Comparison between the observed phase velocities (black dots) and theoretical dispersion curves (blue lines) predicted from the inverted Vs models. (c) Inverted Vs profiles for the dispersion measurements shown in panel (a). Shaded ranges indicate ±1 SD derived from 20 independent GA inversions.

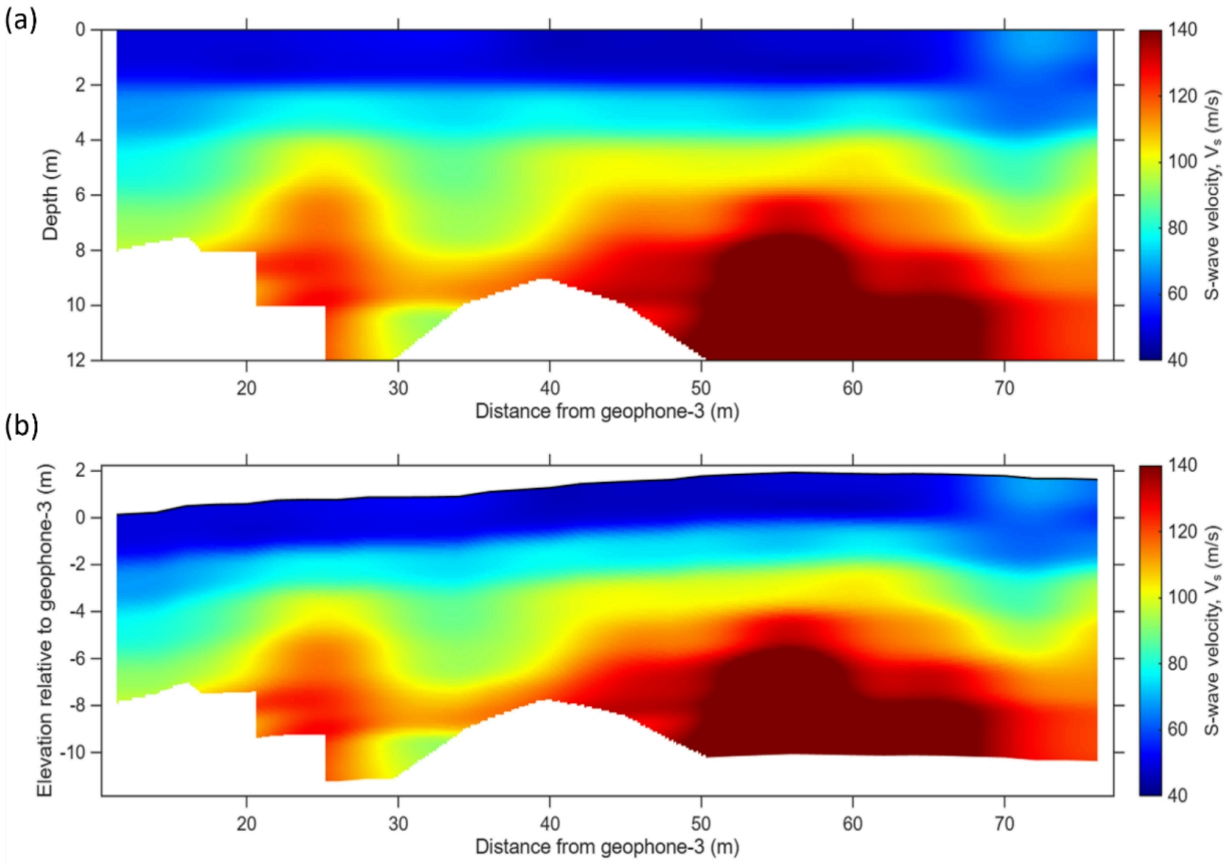


Figure 4

Two-dimensional S-wave velocity structure at Apollo 16 site

(a) Two-dimensional Vs model referenced to depth below the local surface. (b) The same model displayed relative to surface elevation derived from the LROC NAC digital terrain model. Regions outside the reliable depth ranges determined from the sensitivity analysis are shown in white.

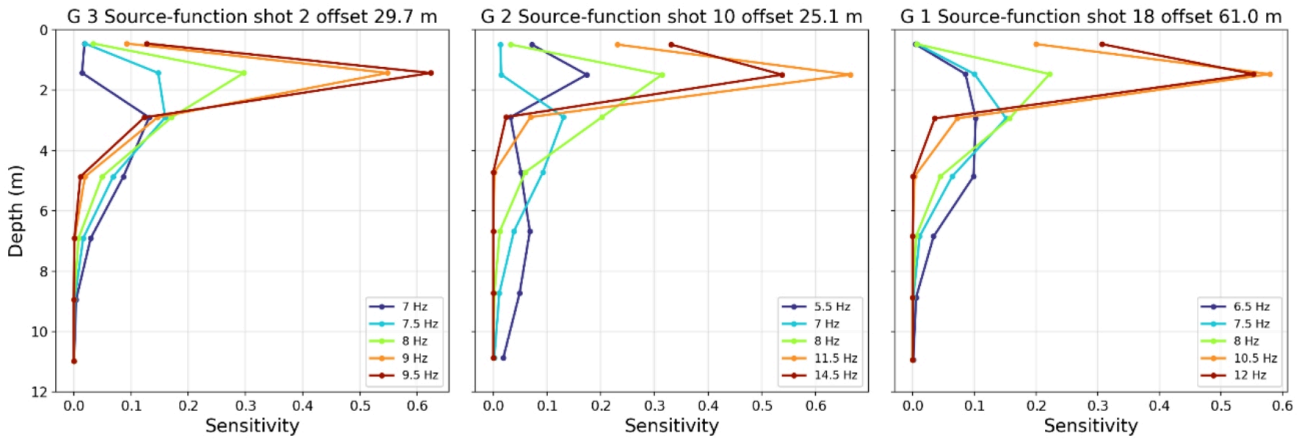


Figure 5

Rayleigh-wave phase-velocity sensitivity to S-wave velocity.
Sensitivity kernels were calculated by finite differences for multiple frequencies. Absolute sensitivity per unit depth is shown as a function of depth. These kernels are for the dispersion curves shown in Fig.3. Higher-frequency measurements predominantly constrain shallow structure, whereas lower-frequency measurements retain sensitivity to greater depths. These kernels were used to determine the reliable depth range of each 1D velocity profile (Fig. 4).

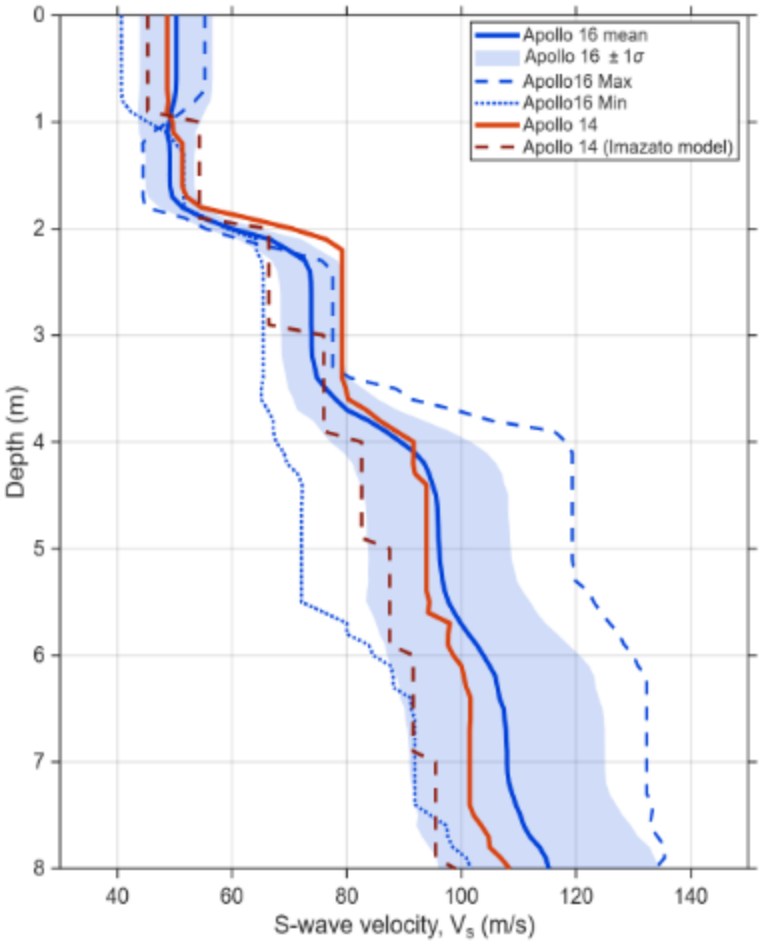


Figure 6

Comparison of S-wave velocity structures at Apollo 14 and Apollo 16 landing sites. The Apollo 16 profile represents the mean of the 1D S-wave velocity models used to construct the 2D section (blue solid line). The blue shaded area indicates ±1σ calculated from these 1D models. The Apollo 16 Max and Min curves represent the individual 1D profiles with the highest and lowest depth-averaged Vs, respectively, over the depth interval of 0–6 m. For Apollo 14, two models are presented to illustrate sensitivity to the initial-model parameterization. The GA model at Apollo 14 site (red solid line) uses the same initial-model construction as that applied to Apollo 16 data, whereas the alternative model follows an initial-model parameterization similar to that of Imazato et al. (2023) (red dashed line).

Supplementary Files

This is a list of supplementary files associated with this preprint. Click to download.

- floatimage7.png